AGU PUBLICATIONS

JGR

Journal of Geophysical Research: Solid Earth

RESEARCH ARTICLE
10.1002/2014JB011526

This article is a companion to *Karlstrom et al.* [2013] doi:10.1002/jgrb.50251.

Key Points:
- Seismic, tilt, thermal, and gravity measurements signals are analyzed
- Water overflowing produces a pressure drop that drives eruption
- A conceptual model for the different stages of eruptive cycle is proposed

Supporting Information:
- Readme
- Texts S1 and S2, Table S4.1, and Figures S3.1–S3.7

Correspondence to:
J. Vandemeulebrouck,
jvand@univ-savoie.fr

Citation:
Vandemeulebrouck, J., et al. (2014), Eruptions at Lone Star geyser, Yellowstone National Park, USA: 2. Constraints on subsurface dynamics, *J. Geophys. Res. Solid Earth*, *119*, doi:10.1002/2014JB011526.

Received 8 AUG 2014
Accepted 28 OCT 2014
Accepted article online 30 OCT 2014

Eruptions at Lone Star geyser, Yellowstone National Park, USA: 2. Constraints on subsurface dynamics

Jean Vandemeulebrouck[1], Robert A. Sohn[2], Maxwell L. Rudolph[3], Shaul Hurwitz[4], Michael Manga[5], Malcolm J. S. Johnston[4], S. Adam Soule[2], Darcy McPhee[4], Jonathan M. G. Glen[4], Leif Karlstrom[6], and Fred Murphy[4]

[1]ISTerre, Universite de Savoie, CNRS, Le Bourget-du-Lac, France, [2]Geology and Geophysics Department, Woods Hole Oceanographic Institution, Woods Hole, Massachusetts, USA, [3]Department of Geology, Portland State University, Portland, Oregon, USA, [4]U.S. Geological Survey, Menlo Park, California, USA, [5]Department of Earth and Planetary Science, University of California, Berkeley, California, USA, [6]Department of Geophysics, Stanford University, Stanford, California, USA

Abstract We use seismic, tilt, lidar, thermal, and gravity data from 32 consecutive eruption cycles of Lone Star geyser in Yellowstone National Park to identify key subsurface processes throughout the geyser's eruption cycle. Previously, we described measurements and analyses associated with the geyser's erupting jet dynamics. Here we show that seismicity is dominated by hydrothermal tremor (~5–40 Hz) attributed to the nucleation and/or collapse of vapor bubbles. Water discharge during eruption preplay triggers high-amplitude tremor pulses from a back azimuth aligned with the geyser cone, but during the rest of the eruption cycle it is shifted to the east-northeast. Moreover, ~4 min period ground surface displacements recur every 26 ± 8 min and are uncorrelated with the eruption cycle. Based on these observations, we conclude that (1) the dynamical behavior of the geyser is controlled by the thermo-mechanical coupling between the geyser conduit and a laterally offset reservoir periodically filled with a highly compressible two-phase mixture, (2) liquid and steam slugs periodically ascend into the shallow crust near the geyser system inducing detectable deformation, (3) eruptions occur when the pressure decrease associated with overflow from geyser conduit during preplay triggers an unstable feedback between vapor generation (cavitation) and mass discharge, and (4) flow choking at a constriction in the conduit arrests the runaway process and increases the saturated vapor pressure in the reservoir by a factor of ~10 during eruptions.

1. Introduction

Geysers, defined as features that episodically erupt liquid and gas, have intrigued scientists for more than a century [*Mackenzie*, 1811; *Bunsen*, 1847; *Le Conte*, 1878]. They provide an excellent opportunity to make geophysical observations because eruption times of some geysers are predictable allowing for optimal instrument setup, and a dense network of instruments can be deployed without safety risks.

Geysers display a great variability in the style, vigor, and duration of their eruptions, with eruption intervals that range from periodic to chaotic [*Rojstaczer et al.*, 2003; *Hurwitz et al.*, 2008, 2014]. Periodic geysers are of special interest because their regularity allows them to be used as natural laboratories for studying the nonlinear feedbacks that control the dynamic behavior of multiphase fluids in eruptive systems.

Despite many theoretical models [e.g., *Rinehart*, 1965; *White*, 1967; *Fournier*, 1969; *Steinberg et al.*, 1981; *Kieffer*, 1989; *Dowden et al.*, 1991; *Ingebritsen and Rojstaczer*, 1993, 1996], laboratory experiments [e.g., *Anderson et al.*, 1978; *Steinberg et al.*, 1982; *Toramaru and Maeda*, 2013; *Adelstein et al.*, 2014], and field measurements [e.g., *Rinehart*, 1965; *Nicholls and Rinehart*, 1967; *Birch and Kennedy*, 1972; *Hutchinson et al.*, 1997; *Shteinberg et al.*, 2013; *Namiki et al.*, 2014] aimed at understanding geysers, we do not understand many of the processes that control the dynamical behavior of periodic geysers, and a number of fundamental questions about their eruptions remain poorly understood. Examples include as follows: how are heat and mass transported from depth into near-surface geyser reservoirs? Are there specific conduit and reservoir geometries required for geyser eruptions? How is energy transferred within the subsurface multiphase flow system? How do eruptions initiate (e.g., by top-down rarefaction waves [*Kieffer*, 1984] or accumulation of steam in a subsurface reservoir ("bubble trap") [*Belousov et al.*, 2013])? How are the preplay pulses of fluid discharge leading up to the eruption related to eruptive processes?

Geophysical surveys of geysers have the potential to address some of these outstanding questions by imaging subsurface processes over large numbers of eruption cycles. Seismic data acquired in the early 1990s demonstrated that Old Faithful geyser in Yellowstone National Park generates hydrothermal tremor that results from collapse of steam bubbles [*Kedar et al*., 1996, 1998]. More recently, the application of ambient noise processing techniques to this data set revealed a previously unknown lateral cavity that appears to exert a major influence on the geyser's eruptions [*Cros et al*., 2011; *Vandemeulebrouck et al*., 2013]. At Old Faithful Geyser of Calistoga, California, tilt measurements have revealed that ground surface deformation around the geyser is in phase with the eruptions [*Rudolph et al*., 2012]. The results of these studies demonstrate how seismic and geodetic measurements can be used to constrain the geometry of the subsurface reservoir and conduit, relate bubble cavitation rates to the eruption cycle, and relate subsurface fluid pressure variations to displacements of the ground surface. Geophysical data sets thus offer insight into spatial and temporal subsurface dynamics that complement downhole measurements of pressure and temperature [e.g., *Birch and Kennedy*, 1972; *Hutchinson et al*., 1997; *Kedar et al*., 1998], visual imaging of conduits [e.g., *Hutchinson et al*., 1997; *Belousov et al*., 2013], and measurements of eruption duration and timing [e.g., *Rojstaczer et al*., 2003; *Hurwitz et al*., 2008, 2012, 2014].

Here we present continuous seismic, deformation (tilt and LiDAR), thermal infrared, and gravity measurements from a 4 day experiment carried out at Lone Star geyser, located 5 km south-southeast of Old Faithful in Upper Geyser Basin (Figure 1), in Yellowstone National Park in September 2010 (Figure 1 and photos in the supporting information), and integrate the results to constrain the key subsurface processes that control the geyser's dynamic behavior. In the Part 1 companion paper [*Karlstrom et al*., 2013], we described measurements and analyses associated with the dynamics of Lone Star geyser's erupting jet. The major observations summarized in that paper are (1) the eruption cycle consists of four distinct phases (eruption, relaxation, quiescence, and preplay) with an average interval of 3:00 h ±0:16 min over 32 consecutive observed eruptions, (2) jet velocities of the eruption fountain range between 16 and 28 m/s with unsteady flow oscillations and intermittent choking at a subsurface nozzle resulting in supersonic flow, (3) the preplay period leading to the eruption is characterized by a series of 5–10 min long steam puffs, (4) the geyser is fed with water that ascends from a deep reservoir with a temperature of 160–170°C, (5) the water volume discharged during an eruptive cycle is $20.8 \pm 4.1\ m^3$, and (6) the total heat output from the geyser is 1.4–1.5 MW. This second paper builds on those results, as well as previous work at Old Faithful geyser [*Rinehart*, 1965; *Nicholls and Rinehart*, 1967; *Kieffer*, 1984; *Hutchinson et al*., 1997; *Kedar et al*., 1996, 1998; *Vandemeulebrouck et al*., 2013], to provide new insight into the dynamic behavior of periodic geysers.

2. Experimental Methods

We acquired contemporaneous, multisensor data from five sites positioned at a variety of azimuths and distances (5–50 m) from the Lone Star geyser cone from 20 to 24 September 2010 (Figure 1b). Infrared and tilt data were acquired at all five sites, gravity data were acquired at two sites, and broadband seismic and acoustic data were acquired at one site. Light Detection And Ranging (LiDAR) scanners were used to generate a detailed digital elevation map of the geyser sinter cone and surrounding features and to attempt to measure ground surface displacements by differencing sequential LiDAR-derived images. We provide a detailed description of the instrumentation in Text S1 in the supporting information. High-speed video, forward looking infrared video, and stream discharge data acquired during the experiment have been described previously [*Karlstrom et al*., 2013].

3. Observations and Results

Here we report results from the seismic, tilt, and thermal measurements. The LiDAR and gravity data are reported in Text S2 in the supporting information because they ultimately did not provide constraints on the geyser's dynamical behavior. Possible ways of modifying the methods employed to acquire the LiDAR and gravity data so as to provide constraints on geyser processes are discussed in section 4.5 and in the supporting information.

3.1. Seismic Records

Seismograms obtained during the study period contain two different signals related to geyser processes: (1) high-frequency hydrothermal tremor in the 1–40 Hz band (Figures 2–6) and (2) ultralong period (ULP)

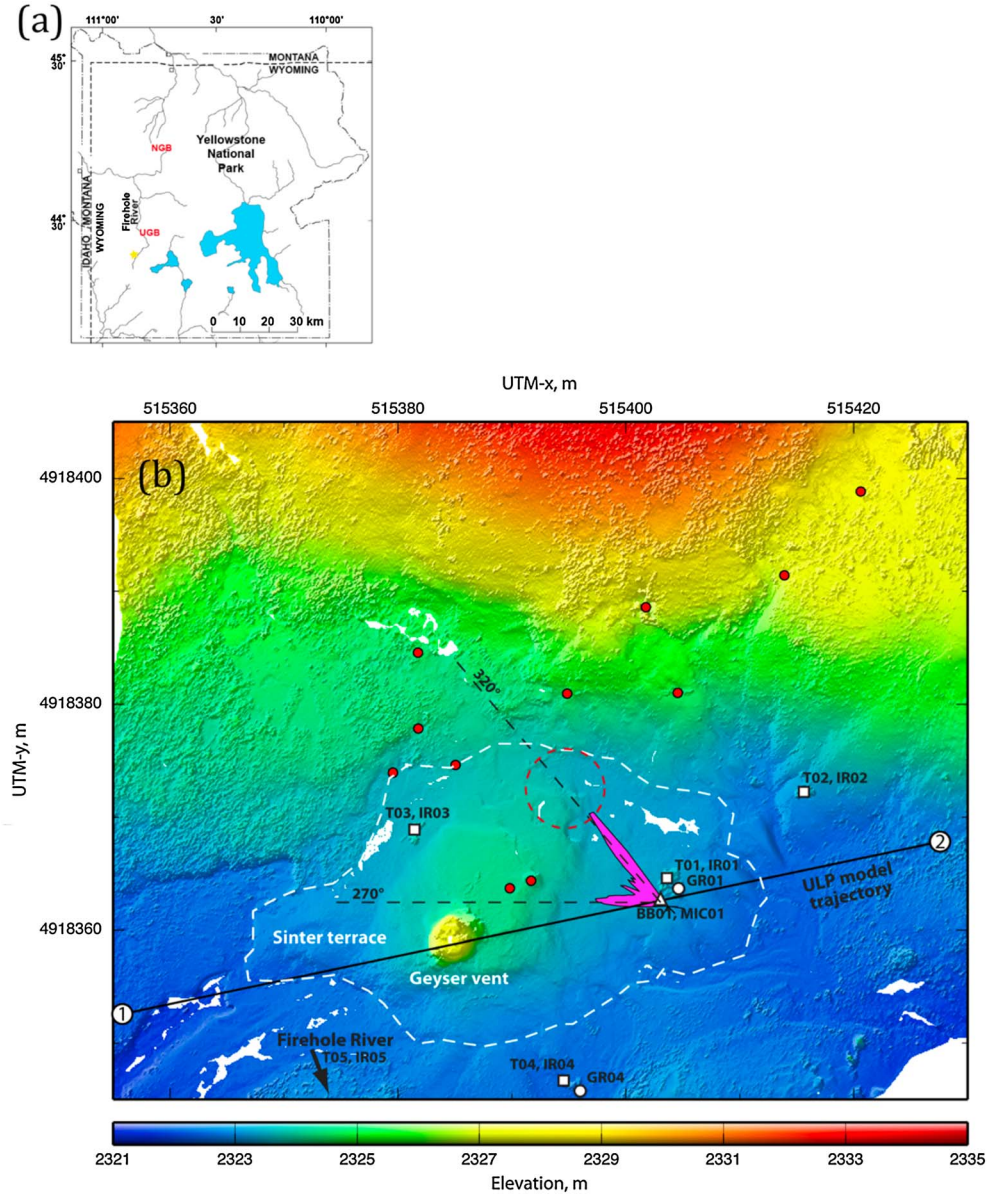

Figure 1. Map. (a) Map of Yellowstone National Park, showing the location of the Upper Geyser Basin (UGB), Norris Geyser Basin (NGB), and Lone Star geyser (yellow star). (b) LiDAR-derived topography of study area. Key features identified on map include: instrument locations as white symbols (T = platform tiltmeter, IR = infrared camera, GR = gravimeter, BB = broadband seismometer, and MIC = microphone), thermal pools are shown as red circles, outline of sinter terrace as dashed white line, ULP source migration model as black line starting at (1) and ending at (2). Rose diagram of hydrothermal tremor back azimuths are shown as magenta vectors originating from BB01 (bin sizes plotted on log scale for scaling). The inferred approximate location of the bubble trap, based on the intersection of tremor back azimuths with the local thermal pool trend, is shown as a dashed, red circle. The Firehole River and the locations of Tilt05 and Infra-red05 are to the south beyond the range of the LiDAR data.

signals with a period of ~120 s (Figure 7). The hydrothermal tremor signals are similar in character to those observed at Old Faithful geyser [e.g., *Kedar et al*., 1998], whereas the ULPs represent a new signal that has not been previously observed in geyser fields.

3.1.1. Hydrothermal Tremor

Seismic energy in the 1–40 Hz band exhibits a tremor-like character with distinct spectral peaks, most prominently at 5–8 Hz and 15–25 Hz (Figure 2a). Following the nomenclature established by *Kedar et al*. [1996, 1998], we refer to these signals as "hydrothermal tremor." Hydrothermal tremor at Lone Star exhibits

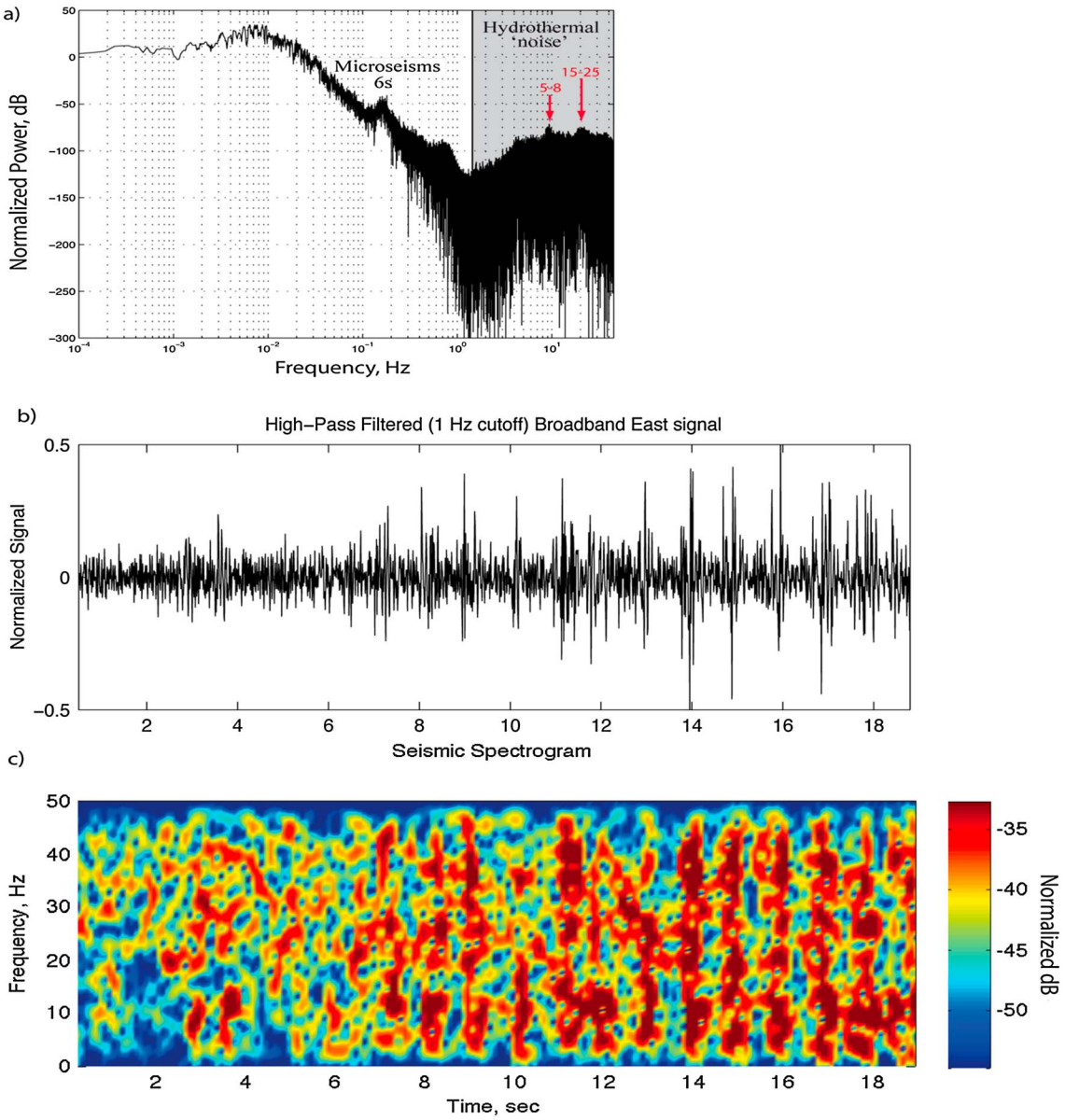

Figure 2. Hydrothermal noise characteristics. (a) Multitaper (*NW* = 2) power spectrum of broadband seismometer data (normalized horizontal E-W component) from one eruption interval (3 h). Above 1 Hz the spectrum is dominated by hydrothermal tremor, with the two strongest peaks in the 5–8 and 15–25 Hz bands, and a third, smaller, peak at 35–45 Hz. (b) High-pass (1 Hz) filtered seismometer data (E-W component) during the onset of cavitation in the preplay phase, before the rate increases to the point where the signal is essentially continuous. Individual bubble collapse events can be seen in both the time series and spectrogram (c) Spectrogram calculated on 0.5 s length windows with 75% overlap.

systematic relationships with the four stages of the eruption cycle described in *Karlstrom et al*. [2013], with remarkably consistent characteristics across all eruption cycles during our observation period (Figure 3). Tremor levels peak at the start of each eruption and then drop to more moderate levels for the duration of the eruptive stage. Immediately following each eruption, tremor levels begin to rise gradually after, with two distinct rise/fall episodes during the relaxation phase (P1 and P2 in Figure 3). Tremor levels are low during the recharge phase and then exhibit sharp peaks corresponding to each of the preplay pulses leading up to the eruption.

Because we used only a single seismometer, we use the polarity of particle motions observed at the sensor to constrain the azimuth of the source(s) relative to the seismic station [e.g., *Falanga and Petrosino*, 2012]. We estimate the polarization direction of incoming tremor signals at the seismometer for both the 5–8 Hz

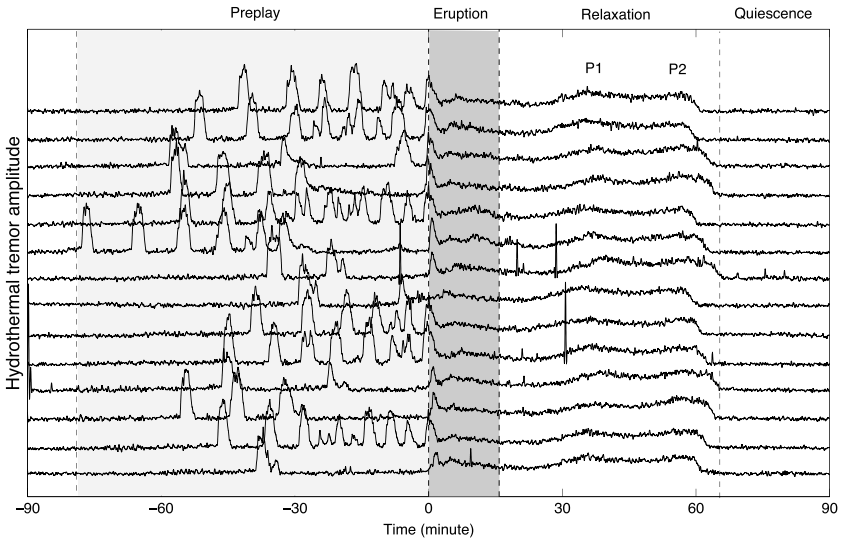

Figure 3. Systematic relationship between hydrothermal tremor amplitude and the four-stage eruption cycle [*Karlstrom et al*., 2013]. Each horizontal trace represents the high-pass filtered (20 Hz) tremor amplitude for one eruption interval (14 total eruptions shown). Time = 0 marks the start of each eruption. Dashed vertical lines indicate the limits of the different stages; preplay stage is shaded in light gray, and the eruption in dark gray. Tremor levels exhibit two broad peaks, P1 and P2 about 35 and 55 min after the eruption, respectively.

and 15–25 Hz frequency bands by diagonalizing the covariance matrix of the three orthogonal velocity components [*Montalbetti and Kanasevich*, 1970] for 12 s time windows over the course of an eruption cycle. We estimate the back azimuth and vertical (dip) angle relative to the seismometer from the eigenvectors and eigenvalues of the diagonalized covariance matrice, along with the rectilinearity

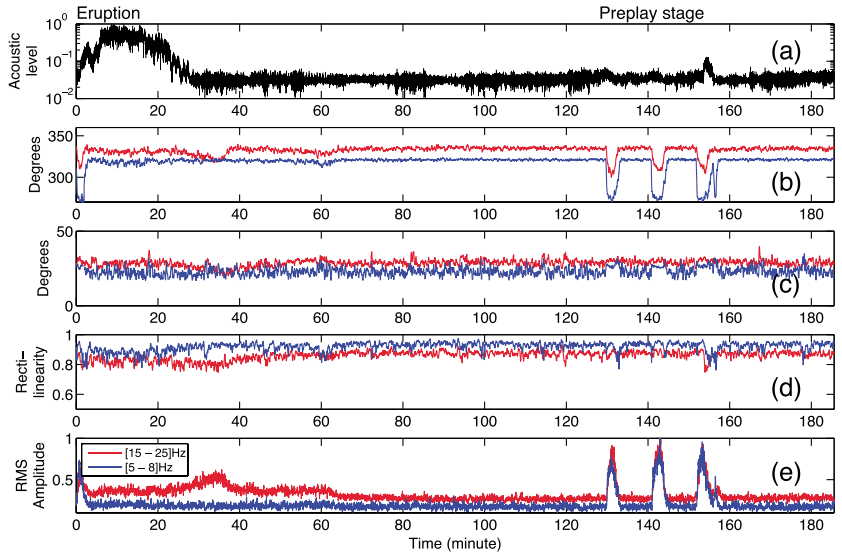

Figure 4. Particle motion polarization analysis of the broadband seismic signal in the 5–8 Hz (blue) and 15–25 Hz (red) frequency bands during one eruptive cycle. Time = 0 refers to the start of the eruption, at 04:49 GMT on 21 September 2010. (a) Normalized RMS level of the acoustic signal recorded by the microphone at Station 1 (Figure 1), (b) horizontal azimuth (degrees), the azimuth of the geyser vent is 270°. (c) dip angle (degrees), (d) rectilinearity parameter indicating the quality of the particle motion analysis, and (e) normalized RMS amplitude of the horizontal seismic velocity (EW component) for the two frequency bands. Note the large amplitude increase during the preplay episodes and the lack of seismic energy released during the eruption in the 5–8 Hz band.

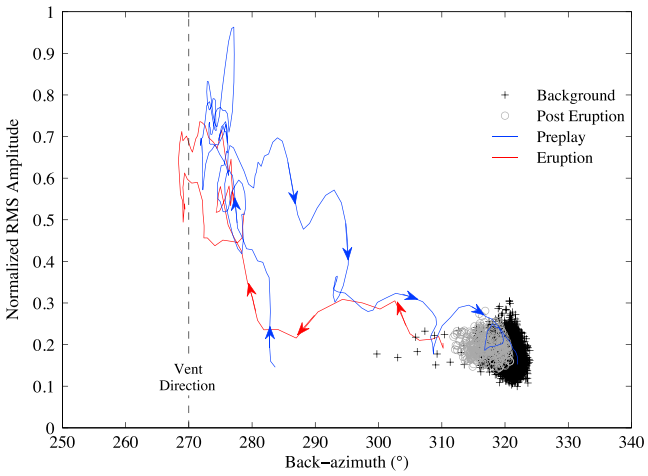

Figure 5. Relationship between tremor RMS amplitude and back azimuth during the eruptive cycle presented on Figure 4. Black crosses correspond to tremor observed during the quiescence/recharge and preplay stages, excluding the high-amplitude preplay pulses. Grey circles correspond to tremor observed during the posteruption stage (P2 in Figure 3). These time windows of low-amplitude tremor constitute the majority of the eruptive cycle. Blue and red lines represent the evolution in tremor back azimuth and amplitude observed during a preplay pulse and at the beginning of the eruption, respectively. The arrows indicate the direction of the temporal evolution. Note that high-amplitude seismic tremor is only observed at back azimuths aligned with the geyser vent.

parameter, $R = 1 - (\lambda_2+\lambda_3)/2\lambda_1$, where $\lambda_1 > \lambda_2 > \lambda_3$ are the eigenvalues (Figure 4). Rectilinearity is a measure of the degree of linear polarization, with $R = 0$ for random data and $R = 1$ for perfectly polarized arrivals.

As with the tremor amplitude, we found systematic relationships between the tremor polarization angle and the phases of the eruption cycle. While the vertical polarization angle does not change much during the eruption cycle (nearly constant at ~25° dip), we observe systematic variations in the back azimuth parameter, indicating lateral changes in the tremor source location. During most of the eruption cycle the tremor source is located to the N-NW of the broadband station at a back azimuth of ~320°N for the 5–8 Hz band and ~335 N° for the 15–25 Hz band (Figure 4b). However, during periods when fluids are being discharged from the geyser cone (i.e., preplay and eruption) the back azimuth to the source changes to ~270°N for the 5–8 Hz band and to ~320°N for the 15–25 Hz band. When the lateral migration of the tremor source during preplay and eruption is examined in detail, we find that the location of the 5–8 Hz source is located at the geyser cone back azimuth when the amplitude initially peaks at the beginning of each pulse, remains at this location for 2 min, and then gradually migrates back to the steady 320°N back azimuth as the amplitude decreases back to background values (Figures 4 and 5). We also find that the 15–25 Hz signal exhibits smaller and more gradual horizontal back azimuth changes of ~10–15° during the rise/fall episodes observed during the relaxation phase (P1 and P2 in Figure 3). This is the only part of the eruption cycle when potentially significant changes in the vertical polarization angle are observed, with the dip angle decreasing by ~10° (i.e., shallowing) relative to background values when the tremor amplitude is highest during the P1 rise/fall episode. Overall, signal rectilinearity is high (>0.8) during most of the eruption cycle, indicating that the tremor signal observed at the seismometer has a well-defined polarization angle.

Finally, there is a time delay between the start of each preplay pulse as indicated by the infrared signal and the corresponding rise in tremor levels (~tenfold amplitude increase over a frequency range of 1–40 Hz for 3–5 min) that systematically decreases leading up to each eruption (Figure 6), at which point the delay effectively becomes zero. The evolution of this time delay leading up to each eruption can be fit (using least squares methods) with an exponential function with a time constant of ~23.4 min. This systematically decreasing delay time between fluid discharge and tremor onset during the preplay phase has not previously been described for other geysers, and we consider the thermodynamic implications in the Discussion (section 4.1).

3.1.2. Ultralong Period Seismic Signals

We observe regular occurrences of self-similar, long-duration (~4 min) signals on the horizontal components of the broadband seismometer (Figure 7). These signals have not been previously reported for geyser systems, and while they bear some similarities to very long period (VLP) signals observed at some volcanic systems [e.g., *Chouet et al.*, 2003; *Sanderson et al.*, 2010; *Kazahaya et al.*, 2011; *Lyons and Waite*, 2011] their duration is much longer (~240 s compared to ~100 s for VLPs) such that we refer to them as Ultralong Period (ULP) events [e.g., *Kanamori and Given*, 1982; *Sanderson et al.*, 2010], though the source processes that produce these signals may differ from those that produce volcanic VLP and ULP events. The average ULP

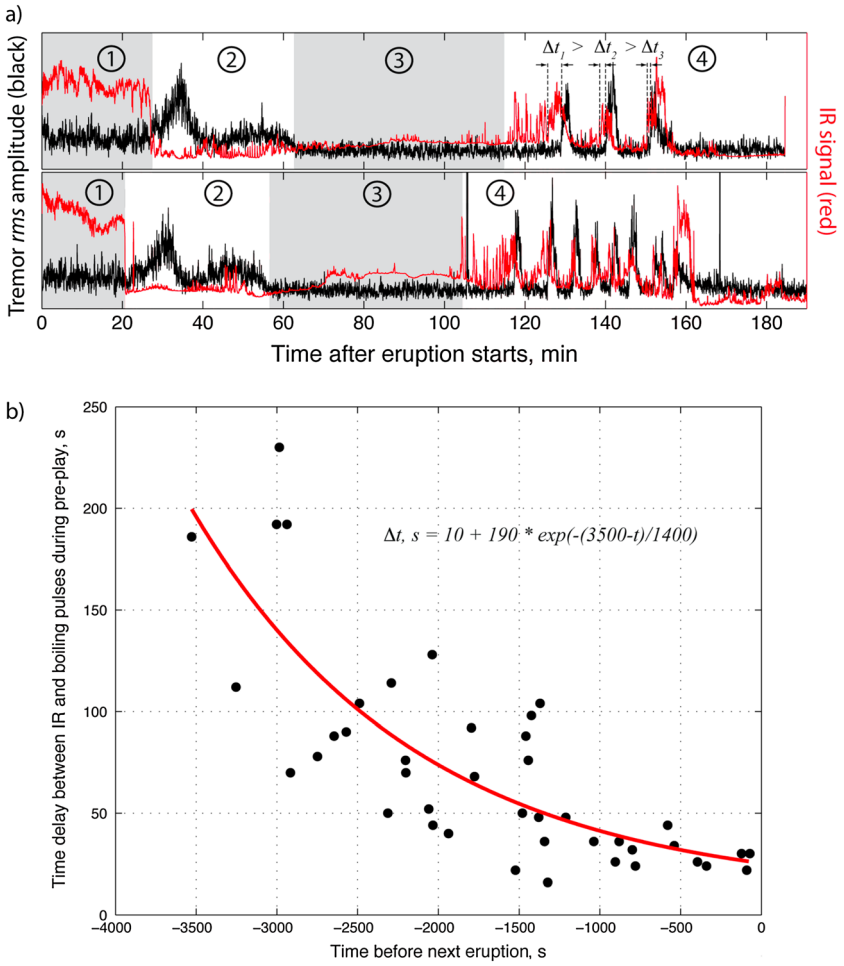

Figure 6. The relationship between the timing of preplay pulses observed in the infrared and hydrothermal tremor time series data. (a) Time series of infrared signal (red) and normalized hydrothermal tremor amplitude (black) over two consecutive eruption intervals (04:49 and 07:54 GMT on 21 September 2010). The four stages of the eruption cycle are shown by shaded rectangles and circled numbers: (1) eruption, (2) relaxation, (3) recharge, and (4) preplay. The decreasing time delay between three successive preplay pulses before the second eruption is shown by vertical dashed black lines. (b) Time delay between the infrared and tremor amplitude pulses as a function of time before the next eruption for the 14 eruption cycles shown in Figure 3 (note that the number of preplay pulses varies between 1 and 8 for these eruptions). The least squares fit of an exponential function to the data (red curve) has a time constant of 23.4 min (1400 s).

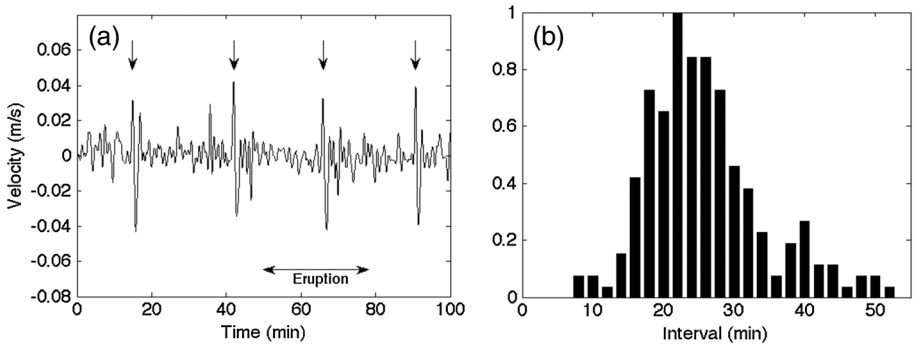

Figure 7. Ultralong Period (ULP) events. (a) Four consecutive ULPs (denoted by arrows) recorded on the east horizontal component of the broadband station. The duration of the eruption starting on 22 September 2010 at 02:41 UT is shown to emphasize that the timing of the ULPs is independent of the eruption cycle. (b) Normalized histogram of recurrence interval for the 199 ULPs studied.

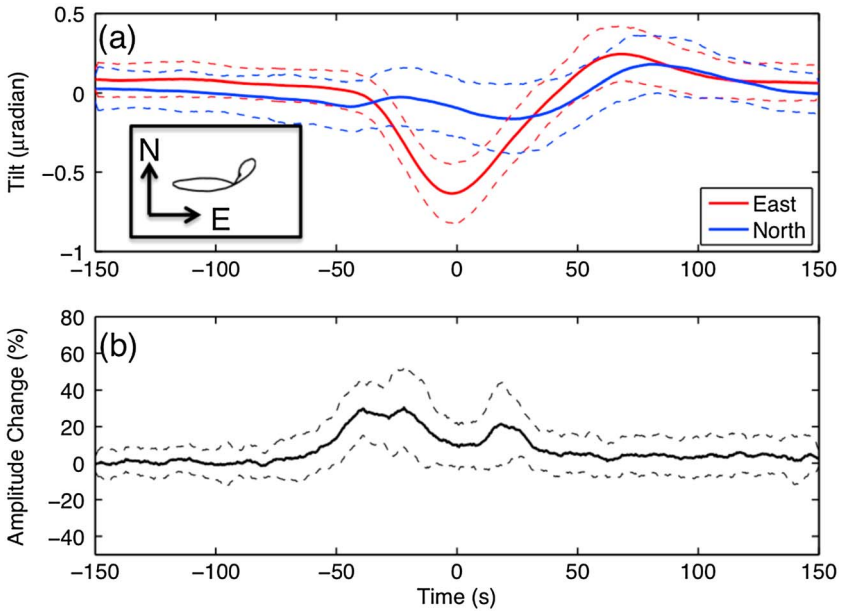

Figure 8. Tilt changes observed by the broadband seismometer during Ultralong Period (ULP) events and associated hydrothermal tremor amplitude changes. (a) ULP tilt transient derived from horizontal mass positions of the broadband seismometer with uncertainties corresponding to 1 standard deviation. Positive numbers correspond to north down tilt (blue) and east down tilt (red) North versus East components. (b) Changes in RMS amplitude of the vertical component of hydrothermal tremor (as a percentage) during the ULP events. The tilt and hydrothermal noise amplitude were averaged for 60 ULP signals.

recurrence period during the first 2 days of the experiment was 26 ± 8 min and then the recurrence time and variability increased slightly (Figure S3.2 in the supporting information). Because the signals were not observed on the vertical seismometer component, we infer that the ULP signals were generated by ground surface tilt (rotation) rather than horizontal displacements (translation). We extract the corresponding tilt vector from the acceleration signals recorded on the horizontal mass positions of the seismometer by dividing the instrument acceleration by the gravity acceleration *g* [*Genco and Ripepe*, 2010; *Sanderson et al*., 2010; *Maeda and Takeo*, 2011; *Lyons et al*., 2012; *Waite et al*., 2013]. All the observed ULP tilt signals are nearly identical with amplitudes of ~1 μrad in the E-W direction and 0.3 μrad in the N-S direction, and durations of ~4 min (Figure 8a). The ULP tilt signals were also observed in records from platform tiltmeter station T01 (located 2 m from the broadband seismometer, Figure 1b), although the data are much noisier and only with stacked waveforms the signals can be resolved. Stacked ULP records from tiltmeter station T01 exhibit changes of 0.12 μrad in the E-W direction and 0.05 μrad in the N-S direction. Although smaller in amplitude, the synchronous tilt records on the platform tiltmeter provide additional evidence that the ULP signals are produced by ground surface rotation rather than horizontal displacement. ULP signals could not be resolved on any of the other platform tiltmeters.

The ULP signals occur randomly with respect to the eruption cycle, and thus appear to be decoupled, at least to first order, from the dynamical behavior of the geyser. Stacks of hydrothermal tremor RMS levels during the ULP cycles suggest that these events may affect tremor amplitude by ~20% (Figure 7b), but we have not been able to identify any relationships between the ULPs and infrared, gravity, and microphone data. The ULPs are thus somewhat enigmatic, and we consider their possible relationship to the geyser system in the Discussion (section 4.2).

3.2. Tilt Transients

Data records from the platform tiltmeters are noisy and exhibit large amplitude variability, and we were unable to extract a spatially or temporally coherent signal related to the eruption cycle. We thus do not use these records in a general sense to constrain the amplitude and location of subsurface pressure changes during the eruption cycle. However, tiltmeter station T03 on the north side of the geyser cone (Figure 1b) exhibits a systematic temporal pattern during the first preplay pulse of each eruption cycle (Figure 9) that is

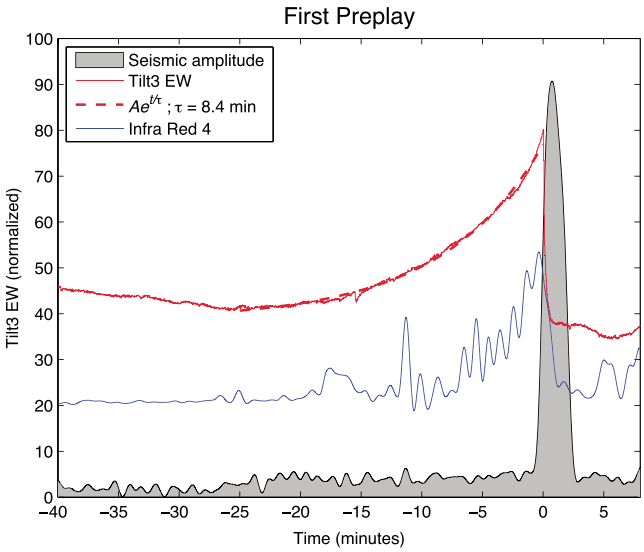

Figure 9. Relationship between tilt, hydrothermal tremor amplitude, and infrared signals during the first preplay episode on 22 September 2010, 07:50 GMT. East-West T03 tilt component is shown by a solid red line, with a least squares fit of an exponential function (time constant: 8.4 min) in dashed red line. Infrared signal IR4 is shown in blue, and the RMS level of hydrothermal tremor in gray. Time $t = 0$ refers to the time at which the tilt amplitude at station T03 and infrared intensity are at maximum. Note the correlated exponential increase on tilt and infrared signals, the periodic thermal pulses at the surface due to water level fluctuations in the conduit and the spectacular rise of the hydrothermal tremor amplitude when both subsidence and water level drop occur.

well correlated with the infrared signal generated by fluid discharge from the vent. The tilt data are best fit by an exponential curve with a time constant of 9 min. After rising, the tilt and infrared signals suddenly drop to their initial values, at which point the hydrothermal tremor RMS amplitude increases by a factor ~20 for 3–4 min.

As described previously, we can use the acceleration signals of the broadband seismometer mass positions recorded at 4 Hz sampling rate to detect tilt patterns. After removing the large diurnal effects with a high-pass filter we find that the horizontal component spectra exhibit a clear peak at ~3 h (~8 cpd), corresponding to the length of the eruption cycle (Figure S3.3 in the supporting information). However, the tilt amplitude and azimuth vary considerably between eruption cycles, likely due to the poor coupling of the sensor with the ground surface and poroelastic and thermoelastic effects in the siliceous sinter layer underlying the sensor. Nevertheless, when we stack records from multiple eruption cycles a fairly consistent pattern can be discerned on the N-S component (Figure 10). The average tilt pattern is essentially stable during the recharge and preplay phases of the eruption cycle, and then drops rapidly during an eruption, before gradually recovering during the relaxation phase. This pattern has the form $A(1 - \exp(t/\tau))$, where A is the tilt amplitude (μrad), t is time (s), and τ is a time constant (s) (Figure 10). A similar tilt pattern was also observed in conduit pressure records, seismicity rate, and hypocentral depth at Old Faithful geyser in Yellowstone [*Kedar et al.*, 1998; *Vandemeulebrouck et al.*, 2013], and in tilt patterns at Old Faithful geyser in Calistoga, California [*Rudolph et al.*, 2012] and Onikobe geyser in Japan [*Nishimura et al.*, 2006]. This pattern is thought to reflect the gradual filling of the geyser reservoir and conduit during the eruption cycle [*Steinberg et al.*, 1981; *Kedar et al.*, 1998]. The time constant of the average Lone Star geyser tilt transient is 45 min, compared with the 34 min pressure transient in the conduit of Old Faithful geyser [*Kedar et al.*, 1998].

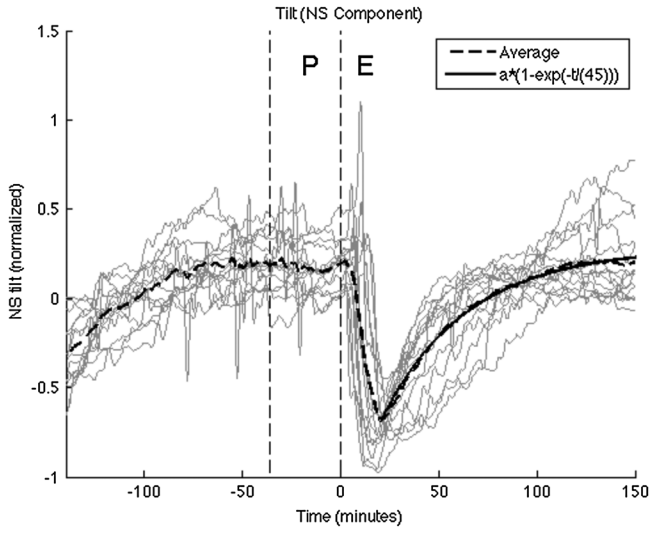

Figure 10. Normalized north-south tilt component on the broadband seismometer versus time during 14 eruptive cycles (in light gray). Time = 0 marks the start of the eruption (*E*) and *P* corresponds to the preplay phase. The average tilt is shown as a black dashed line, and an exponential fit to the recovery following the eruption is shown in black (time constant $\tau = 45$ min).

4. Discussion

The geophysical data we have acquired provide new insight into the dynamical behavior of periodic geysers. We begin by discussing the potential tremor-generating mechanisms and describe how the tremor amplitude and the timing of the preplay pulses can be used to constrain thermodynamic conditions in the geyser system. We then develop a model for the ULP signals observed on the broadband seismometer and discuss their relationship to the geyser system. We conclude by discussing the role of trapped, pressurized vapor on the dynamic behavior of the system, and how thermomechanical feedback between the various system components controls many aspects of the system dynamics.

4.1. Hydrothermal Tremor

4.1.1. Source Mechanisms

Analysis of seismic signals recorded on the broadband station gives evidence of a permanent hydrothermal tremor at Lone Star, whose level varies during the eruptive cycle, with a spectacular increase during the preplay and eruptive stages. Hydrothermal tremor in geysers is generated by impulsive pressure signals associated with collapsing vapor bubbles [*Kedar et al*., 1998]. Bubble "collapse" refers to the momentary large pressures generated when the bubble contents are highly compressed, which occurs both when bubbles are destroyed and when they are nucleated (owing to the rebound that follows overexpansion during nucleation). Seismic energy is generated when the impulsive pressure perturbation in the liquid couples into the elastic matrix surrounding the fluid [*Thiéry and Mercury*, 2009], and these impulsive events are superposed to create a tremor-like effect when rates are high [e.g., *Kieffer*, 1984; *Kedar et al*., 1996, 1998]. Tremor-generating bubble collapse in a geyser system can occur in three different scenarios: (1) bubble nucleation, (2) bubble collapse at an interface, and (3) vapor condensation in a subcooled liquid. We review each of these three scenarios in the context of the data we acquired at Lone Star geyser.

Vapor bubbles can nucleate in a liquid when its pressure decreases below the saturated vapor pressure (termed "cavitation") or when temperature increases above the saturation temperature (termed "boiling"). In both cases the void space required to form a vapor bubble is created by rupturing the liquid, which generates an impulsive pressure signal [e.g., *Brennen*, 1995]. Bubble nucleation is therefore a plausible mechanism for hydrothermal tremor. Cavitation (nucleation via decrease in pressure) is of special interest in a geyser because system-wide pressures can drop nearly instantaneously when mass is discharged from the system, and localized pressure drops can also occur during periods of flow (e.g., Bernoulli effect and turbulence). In contrast, thermal signals diffuse relatively slowly through the system since the thermal inertia of water is high and the walls of the geyser cavities/conduits act as sinks that continually remove heat from the system via conduction. According to these two different timescales, we attribute the sharp rise in tremor level observed at Lone Star during the preplay pulses (Figures 4e and 5) as the result of a sudden pressure decrease rather than a slow temperature increase. The intensity of the acoustic emissions during cavitation, and thus the tremor amplitude, is largely controlled by the nucleation rate [*Morozov*, 1969]. The total pressure field can be viewed as a superposition of the perturbations caused by individual nucleation events unless the bubble population densities are very high [*Baiter et al*., 1982]. The nucleation rate is controlled by the magnitude of the pressure drop, Δp, relative to the saturated vapor pressure (i.e., $\Delta p = p_\infty - p_{sat}(T_\infty)$, where p_∞ is the ambient fluid pressure, and $p_{sat}(T_\infty)$ is the vapor saturation pressure at the ambient fluid temperature). This relationship allows us to use tremor amplitude as a first-order proxy for the difference between ambient and saturated vapor pressures in cases where nucleation occurs by cavitation.

The second and third scenarios listed above (collapse at a free surface and collapse due to condensation) represent the two possible fates of vapor entering the geyser system. As we shall discuss below, our model for the Lone Star plumbing system includes a bubble trap that is laterally offset from the eruption conduit such that a vapor bubble rising into the system cannot escape to the atmosphere but instead will be trapped in a subsurface cavity [*Mackenzie*, 1811; *Belousov et al*., 2013]. In general, the bubble trap will be filled with time-varying proportions of liquid water and vapor separated by a free surface. There are two possible fates for a rising vapor bubble: (1) the bubble may rise through the subcooled liquid and collapse/burst at the free surface formed by the water/vapor interface and subsequently accumulate in a pocket under the roof of the cavity, or (2) a vapor bubble may condense upon encountering subcooled liquids. Collapse of a vapor bubble at a free surface generates impulsive pressure perturbations [*Blake and Gibson*, 1981; *Blake et al*., 1987], including reentrant jets (that are responsible, for example, for the splashing often observed in thermal pools and pots of boiling water), and is thus a plausible tremor source mechanism.

In the second case, the dynamical behavior of a vapor bubble collapsing in a subcooled liquid is largely controlled by the degree of subcooling [e.g., *Chen and Mayinger*, 1992]. If the degree of subcooling is high, then the collapse rate is controlled by the liquid inertia (i.e., inertial mode oscillations), which results in a rapid/violent collapse that can generate impulsive pressure perturbations. Alternatively, if the degree of subcooling is low, then the collapse rate is controlled by heat flux across the bubble wall (i.e, thermal mode oscillations), which results in a slow and gentle collapse that will not generate tremor. The relative importance of inertial versus thermal mode dynamics in this kind of scenario is represented by the dimensionless parameter, B, defined by

$$B = Ja^2 \frac{\kappa_{\mathrm{TL}}}{R_0} \sqrt{\frac{\rho_L}{p_\infty - p_{\mathrm{sat}}(T_\infty)}}, \tag{1}$$

where κ_{TL} is the thermal diffusivity of the liquid, R_0 is the bubble radius, ρ_L is the liquid density, p_∞ is the ambient fluid pressure, $p_{\mathrm{sat}}(T_\infty)$ is the vapor saturation pressure at the ambient fluid temperature, and Ja is the dimensionless Jacob number representing the degree of subcooling of the liquid [*Florschuetz and Chao*, 1965]. Ja is given by

$$Ja = \frac{\rho_L}{\rho_V} \frac{c_{pL}(T_{\mathrm{sat}}(p_\infty) - T_\infty)}{h_{fg}}, \tag{2}$$

where c_{pL} is the specific heat of the liquid, ρ_v is the vapor density, h_{fg} is the latent heat of evaporation, $T_{\mathrm{sat}}(p_\infty)$ is the vapor saturation temperature at the ambient fluid pressure, and T_∞ is the ambient fluid temperature. Theoretical and experimental results have shown that inertial mode oscillations occur for values of $B \geq 0.3$, thermal mode oscillations occur for $B \leq 0.03$, and transitional behaviors are observed for intermediate values [*Florschuetz and Chao*, 1965]. When thermodynamic parameters appropriate for vapor condensation at Lone Star are substituted into these equations (see Appendix A), we find that collapse of a condensing vapor bubble is expected to occur in the thermal mode, and that vapor condensation is thus unlikely to generate hydrothermal tremor.

The tremor frequencies that we observed fall in the range $1 \leq f \leq 40$ Hz, with distinct peaks at 5–8 Hz and 15–25 Hz. An idealized model relating the frequency content of seismic energy radiated by a collapsing bubble to bubble size [*Rayleigh*, 1917] yields bubble sizes of ~0.5 m for the tremor frequency range of ~20 Hz observed both at Lone Star and Old Faithful, which is unrealistically large (e.g., larger than the eruption conduit dimensions) [*Kedar et al*., 1998]. Some sort of damping mechanism must be added to the idealized Rayleigh model to reduce the oscillation frequency to the values observed both at Lone Star and Old Faithful. *Ichihara and Nishimura* [2009] proposed that damping from mass exchange between the liquid and the bubble via evaporation/condensation (i.e., phase changes) at the bubble wall may explain the frequency mismatch between observations and theory, but this issue has not yet been resolved. In addition, bubble-bubble interactions in a bubble cloud can also exert a significant influence on oscillation frequencies [e.g., *Yoon et al*., 1991].

4.1.2. Tremor Source Migration

Particle motion polarization based on a single seismometer reveals that during most of the eruption cycle the tremor source is located at back azimuths of 320–330°N (Figure 1b), i.e., not beneath the geyser cone. However, during preplay pulsing and at the beginning of each eruption (i.e., when fluids are being discharged from the cone), the tremor source location is likely located within the eruption conduit. At the end of the discharge periods, the tremor source location gradually migrates back to the original source region over a period of ~2 min (Figures 4 and 5). This is consistent with the superposition of tremor signals from two discrete source locations. First, a steady, low-amplitude source at the 320°N back azimuth and second, a transient, high-amplitude source close to the 270°N back azimuth. Alternatively, there could be a single source region that jumps to the 270°N back azimuth and then gradually migrates back to 320°N. Regardless of the cause of the apparent migration, it is clear that the geyser plumbing system is not localized directly beneath the exit vent/cone. There is a region to the NW of the geyser cone that generates steady levels of tremor, and this is a key piece of evidence informing the subsurface geometry of the geyser's conduit system. These lateral migrations of the tremor source during preplay and eruption are similar to observations and inferences from Old Faithful geyser [*Vandemeulebrouck et al*., 2013], supporting the concept of a reservoir or bubble trap that is laterally offset from the geyser cone. Such plumbing system

geometry is consistent with observations from Old Faithful Geyser and supports a bubble trap model [e.g., *Mackenzie*, 1811; *Belousov et al*., 2013] where fluids enter the system through a subsurface cavity and exit through an eruption conduit that is laterally offset from the bubble trap (Figure 13a).

The steady, low-amplitude tremor observed from the 320–330°N back azimuths is most consistent with the collapse of incoming vapor bubbles at the liquid/gas interface in a laterally offset bubble trap. The other possible mechanism, bubble nucleation, is difficult to reconcile with the fact that ambient fluid pressures in the system are probably increasing (from fluid input) during these periods of steady tremor. Thus, we hypothesize that there is a steady tremor source in a laterally offset bubble trap during essentially the entire eruption cycle as incoming vapor bubbles collapse at the liquid/gas interface and accumulate under the roof of the subsurface cavity.

The stepwise shift of the tremor source back azimuth during preplay pulse and eruption (Figures 4 and 5) is accompanied by a ~20 times increase in amplitude, indicating the occurrence of an energetic acoustic emission during periods when fluids are discharged from the geyser system. Mass discharge reduces ambient fluid pressure, such that these high-amplitude tremor pulses can be explained by cavitation (bubble nucleation from a pressure drop) in the eruption conduit. This process, however, does not shut off the input of vapor to the bubble trap, such that high-amplitude cavitation tremor from the eruption conduit is superimposed on the steady, lower amplitude tremor from the bubble trap. The polarization angle of the superimposed signals thus depends on the relative amplitude of the two sources, and we can see in Figure 4 that the rectilinearity parameter decreases during the preplay pulses and eruption, consistent with this hypothesis. At the end of these pulses, the tremor back azimuth slowly migrates back to the original position, which we interpret as a gradual reduction to zero of the tremor amplitude in the eruption conduit. This gradual, lateral migration is difficult to explain with a single, migrating source because the pressure perturbations triggering cavitation propagate nearly instantaneously (i.e., sound speed in the medium) through the system, which is inconsistent with the gradual shift in polarization angle.

4.1.3. Time Delay in the Onset of Tremor

During preplay pulsing there is a time delay between the discharge of fluids from the geyser cone (as inferred from the infrared signal) and the onset of hydrothermal tremor that systematically decreases in a roughly exponential fashion (with a time constant of ~23 min) leading up to eruption (Figure 5). As described in section 4.1.1, the susceptibility to cavitation is primarily a function of the difference between the ambient (reservoir) pressure and the vapor pressure at the reservoir temperature (i.e., $\Delta p = p_\infty - p_v(T_\infty)$), such that the pressure drop required to trigger cavitation in a subcooled liquid decreases as the temperature, and thus the vapor pressure, increases. This suggests that the decreasing time delay between the infrared and tremor signals results from a systematic increase in eruption conduit fluid temperature leading up to an eruption, which in turn systematically decreases the volume of fluid that must be removed from the system before triggering cavitation during discharge events. In this sense we may consider the preplay pulses to represent failed eruptions. Fluids pulse out of the system once the conduits are full, but eruptions only begin once the eruption conduit fluids are hot enough (at or near the boiling temperature) to immediately cavitate upon the removal of an incremental load. The systematic increase in fluid temperature is likely due to the release of latent heat from condensation of steam bubbles entering the conduit system.

4.2. ULP Seismic Signals

The ULP signals we observed, with recurrence intervals ranging from 8 to 53 min and a mean value of 26 min, represent a previously unknown type of deformation associated with the geysering process. Whereas the 32 geyser eruption intervals observed during the experiment were nearly uniform (3:00 h ± 0:16 min), the 199 ULP events we recorded occurred randomly throughout the eruption cycle and did not appear to affect the dynamical behavior of the geyser except to incrementally suppress the amplitude of hydrothermal tremor (Figure 8).

We hypothesize that the ULPs are generated by the slow ascent of vapor slugs [e.g., *James et al*., 2004, 2006; *Balmforth et al*., 2005; *Rust et al*., 2008] beneath the sinter cone. This model is conceptually different from models for VLP and ULP signals at volcanoes that are typically attributed to spatially fixed, time-varying seismic sources [e.g., *Ohminato et al*., 1998; *Chouet et al*., 2003, 2005; *Ohminato*, 2006; *Lyons and Waite*, 2011; *Maeda et al*., 2013; *Chouet*, 2013]. In our conceptual model (Figure 11), a bubble or slug of steam travels

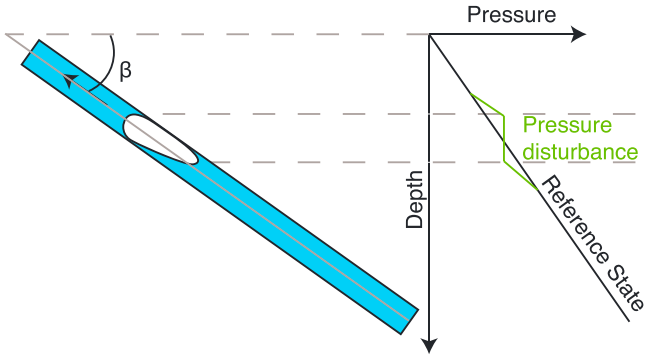

Figure 11. Schematic illustration of the bubble that drives ULP tilt signals (left) and the conceptual model for pressure changes driving ground deformation (right).

through an inclined conduit, and we model the slug as a pressure disturbance that propagates along a fixed trajectory. We illustrate two possible perturbations to the reference pressure state (black line in Figure 11), which is assumed to be hydrostatic. Owing to the low density of the gas or steam relative to liquid water, we treat the bubble as isobaric. If we assume that far away from the bubble, pressure returns to hydrostatic values, the pressure perturbation is expected to resemble the green curve in Figure 11. We approximate this pressure disturbance as a pair of point pressure sources [*Mogi*, 1958] with fixed separation and opposite sign. We assume that the propagation trajectory is a straight line characterized by an azimuth, α (°), plunge, θ (°), and propagation velocity, v (m · sec^{-1}), with constant strength $s = a^3\Delta P/G$ where a (m) is source radius, ΔP (Pa) the pressure change, and G (Pa) is the elastic shear modulus. We assume that the source trajectory passes through the origin of a model coordinate system and treat the x-y position of the observer (T01 in Figure 1b) as an unknown. To find an optimal set of the eight free parameters, we employed a hybrid global optimization procedure combining simulated annealing with a direct global optimization procedure (pattern search) to minimize the misfit in the L2-norm between the observed and modeled tilt vectors. The global optimization procedure was repeated several hundred times with random initial guesses.

We list the parameters that define the optimal model in the supporting information (Table S4.1) and show the observed versus the best fitting model tilt in Figure 12. The horizontal trajectory of the best fitting model is shown in Figure 1b. The sensitivity of the residual to each source parameter in the region near the optimal solution is shown in Figure S3.6 in the supporting information. In general, the residual is more sensitive to changes in depth, x position of the propagation path, and velocity, and less sensitive to similar fractional changes in plunge, strength, y position of the propagation path, and separation of the positive and negative pressure anomalies. We note that the y position of the source is essentially unconstrained by the inversion, which means that the N-S position of the trajectory in Figure 1b is somewhat arbitrary. For simplicity, we have aligned the trajectory with the geyser cone, but this is not required to fit the data. The propagation path is very slightly upward (0.15°), qualitatively consistent with the very slow propagation velocity of 0.2 m · s^{-1}.

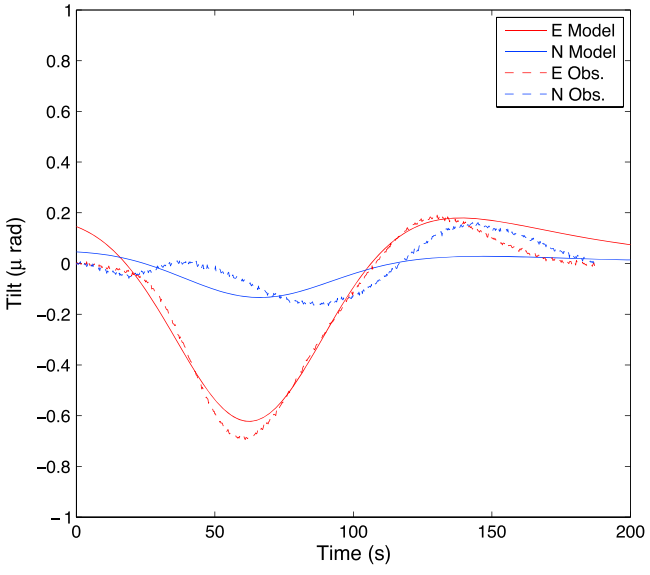

Figure 12. Best fit modeled (solid) and observed (from Figure 8, dashed lines) ULP tilt signals for optimal source parameters listed in Table S1 in the supporting information. The sensitivity of misfit to observed ULP tilt signal for all parameters considered in the tilt source model is presented in Figure S3.6 in the supporting information.

Spatially fixed seismic sources require more free parameters (six moment tensor components and three force components), each of which is allowed to vary in time. In comparison, our model has only eight free parameters

and these do not vary in time. Because the amplitude of the ULP tilt signal is quite large (~1 μrad), a conceptual model involving modest pressure changes (smaller than hydrostatic pressure) must place these pressure changes at relatively shallow depths (no more than a few tens of meters).

Although volcanic VLP and ULP events can sometimes be linked to gas emission at the vent [*Kazahaya et al*., 2011; *Patrick et al*., 2011; *Waite et al*., 2013], we found no evidence for increased temperature (measured with infrared video) at the vent coincident with the ULP signals. Because the ULPs did not appear to affect the dynamical behavior of the geyser, except to incrementally suppress the amplitude of hydrothermal tremor, their relationship to the geyser system is not obvious.

4.3. Flow Oscillations

As described in *Karlstrom et al*. [2013], Lone Star geyser exhibits dynamic flow oscillations during the preplay stage leading up to an eruption, during an eruption, and during the relaxation stage after an eruption. Specifically (1) during eruption the flow velocity oscillates at a period of ~20 s, (2) during relaxation the fluid level in the eruption conduit oscillates at a smoothly varying period of ~30–40 s, and (3) during preplay the fluid level in the eruption conduit oscillates at a smoothly varying period of ~50–70 s. Oscillations with similar periods have been observed at Old Faithful Geyser with a video camera lowered into the conduit [*Hutchinson et al*., 1997] and at the location of hydrothermal tremor sources [*Vandemeulebrouck et al*., 2013]. This dynamical behavior is consistent with hydraulic loading of a pressurized two-phase (liquid/vapor) mixture, as we describe below.

Thermal water sourcing the Upper Geyser Basin ascends adiabatically from an overpressured reservoir at 160–210°C [*White et al*., 1975; *Fournier*, 1989; *Hurwitz et al*., 2012; *Hurwitz and Lowenstern*, 2014]. At Lone Star, ascent and decompression nominally produces ~12 wt % vapor at the ground surface pressures [*Karlstrom et al*., 2013] such that mass flux into the system occurs as a mixture of vapor and liquid entering the bubble trap.

The bubble trap provides storage for thermodynamic and mechanical energy in the form of pressurized vapor, which is primarily released during eruption, but also during relaxation and preplay. As described in section 4.1, vapor entering the bubble trap may condense or ascend through the liquid volume, collapse at the liquid/vapor interface, and then enter a vapor pocket beneath the cavity roof. It seems likely that most vapor traverses the liquid without condensing given that (1) the bubble trap liquids should be near saturation conditions (i.e., little-to-no subcooling) at all times since they presumably enter as an equilibrium mixture of liquid and vapor, and heat loss via conduction and advection to other parts of the system is balanced by heat input from below, and (2) the essentially continuous, low levels of hydrothermal tremor (Figures 4e and 5) observed throughout the eruption cycle to the north-northeast of the geyser cone (back azimuth of ~320–335°N to the seismic station) are consistent with vapor bubbles collapsing at the liquid/vapor interface as opposed to condensing in the liquid.

Liquids entering the system may flow through the bubble trap and lateral conduit into the eruption conduit in order to maintain hydrostatic equilibrium between the eruption conduit and the bubble trap. Vapor entering the system, however, cannot escape the bubble trap (unless it condenses), and thus the vapor mass in the bubble trap will steadily grow. During the recharge phase of the eruption cycle the bubble trap is only partially full of liquid and vapor, and the free surface interfaces in both the eruption conduit and the bubble trap are equal to atmospheric pressure (regardless of absolute depth). However, once the volume of the liquid and vapor mixture in the bubble trap is equal to the volume of the bubble trap, itself, any subsequent addition of mass (either liquid or vapor) will cause the vapor to compress. Consider the conditions when the vapor volume, V_{V0}, and the liquid volume, V_{L0}, in the bubble trap sum to the volume of the bubble trap (Figure 13b, left). The liquid level in the eruption conduit, h_0, is in hydrostatic equilibrium with the pressure in the bubble trap, which will depend on the relative mass fractions of vapor and liquid in the system at this time. This equilibrium fluid level in the eruption conduit can vary during the eruption cycle, and from one eruption cycle to the next. The rise of water level observed before the preplay pulses (Figure 9) increases the hydrostatic pressure in the bubble trap, which likely generates the synchronous surface tilt transients (Figure 9) that are composed of an exponential increase followed by a sudden drop at the time when cavitation begins. The exponential rise of both water level and tilt could be explained by thermal expansion of fluids in the system.

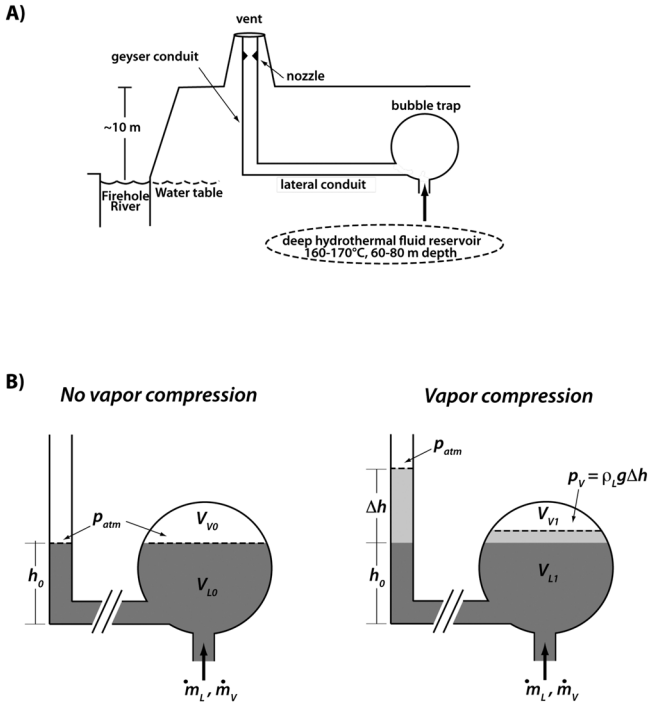

Figure 13. Conceptual model for geyser dynamics. (a) Schematic drawing of subsurface plumbing system. Four components are essential for modeling the observed dynamic behavior: geyser conduit, nozzle, lateral conduit, and bubble trap. Thermal fluids enter the system through the bubble trap and exit through the geyser vent. The system is assumed to be isolated from other sources of fluid input (e.g., groundwater) and is likely perched above the nearby Firehole River. (b) Dynamic coupling between the geyser conduit and the bubble trap (see text for explanation of variables). Vapor is trapped in the bubble trap and compressed by the hydrostatic load of geyser conduit fluids. The compressed vapor stores thermal and mechanical energy that is released during eruptions and relaxation.

Now consider conditions after an incremental time step when both liquid and vapor flux into the bubble trap $(\dot{m}_L, \dot{m}_V)$. The liquid level in the eruption conduit rises by an incremental amount, Δh, but now, while the pressure at the free surface in the eruption conduit is still atmospheric, the trapped vapor in the bubble trap compresses in response to the incremental load, $\rho_L g \Delta h$. Thus, the compressed vapor volume in the bubble trap acts as a spring that is loaded by the fluid in the eruption conduit, and this provides a model for the flow oscillations of several tens of seconds period observed during preplay (Figure 9), eruption, and relaxation (see *Karlstrom et al.* [2013], Figure 5). Once the vapor becomes compressed the saturation temperature will begin to increase, which will modulate mass flux from evaporation/condensation at the vapor/liquid interface in the bubble trap, and this will affect the liquid, V_{L1}, and vapor, V_{V1}, volumes as the system evolves.

The oscillation period, T (s), of this mass-spring system is given by

$$T = 2\pi\sqrt{\frac{V\beta\rho_l\Delta h}{A}} \qquad (3)$$

where V is the compressible volume (m^3), β the compressibility of the fluid (Pa^{-1}), ρ_l and Δh are the density ($kg\,m^{-3}$) and height (m), respectively, of the liquid column, and A (m^2) is the cross section of the conduit. Assuming that liquid density and cross-sectional area are constant to first order, then the oscillation period of this system depends on the compressibility and volume of the two-phase mixture, V, and the height of the water column above the equilibrium position, Δh (i.e., the load). The compressibility of a two-phase mixture is greater than the compressibility of pure steam, and it depends on the relative mass fractions of liquid and vapor (Figure S3.7 in the supporting information) [e.g., *Grant and Sorey*, 1979]. In addition, the compressibility is also a function of the load, Δh, which modulates the saturation pressure and temperature of bubble trap liquids. The dynamic behavior of the coupled eruption conduit-bubble trap system is thus complex, but we can see that the oscillation period primarily changes in response to changes in liquid/vapor mass fractions (compressibility) and load, assuming that the compressible volume of the bubble trap two-phase mixture is constant (i.e., equal to the bubble trap volume).

Qualitatively, the progression from longer (~60 s) periods during preplay to shorter (~20–30 s) periods during eruption and relaxation is consistent with an increase in the vapor mass fraction in the bubble trap in response to the pressure drop associated with mass discharge from the system and/or a reduction in load. Substituting plausible values for conduit diameter (area) into equation (3), we find that the 60 s oscillations observed during preplay are consistent with values of 6–70 m^4 for the product $V\Delta h$, depending on saturation temperature and the relative proportions of vapor and liquid forming the compressible mixture. The reduction in oscillation period to 30 s during posteruption relaxation is consistent with the withdrawal of water mass during the eruption ($V\Delta h$ decreases by factor of 3–10). These $V\Delta h$ values are of the

proper scale for a shallow geyser system, indicating that the mass-spring model provides a plausible explanation for the flow oscillations observed leading up to, and immediately following, each eruption. These water level oscillations in the conduit play an important role in the preplay dynamics as they increase the amplitude of the dynamic pressure variations that trigger cavitation and vapor generation.

4.4. The Geyser Conduit Nozzle and Implications of Flow Choking

The presence of a nozzle or constriction in the eruption conduit plays a key role in generating the eruption fountain [*Karlstrom et al*., 2013] and pressurizing the reservoir. As fluids flow through the nozzle they experience a pressure drop (and acceleration) proportional to the change in cross-sectional flow area. If the fluid is close enough to saturation conditions then this pressure drop triggers cavitation in the constriction, and fountaining is initiated by volume expansion associated with vapor generation. In this sense the nozzle acts as a siphon that reduces pressure at the vent and increases fluid discharge rates out of the system, which in turn initiates an unstable feedback with vapor pressure in the bubble trap as the cavitation rate increases in response to unloading. As the eruption progresses, the pressure difference between the nozzle exit and the vapor pressure in the bubble trap rapidly increases until the nozzle becomes choked. Once the nozzle is choked, mass flux cannot increase further but vigorous cavitation continues in the bubble trap and vapor pressure continues to grow.

In this sense, we can conceptualize the nozzle as a valve that turns the bubble trap into a pressure cooker. We do not have any direct measurements of the overpressure that develops in the bubble trap, but *Karlstrom et al*. [2013] estimated a vent exit pressure of 1.2 MPa based on the expansion angle of fluids discharging from the cone during the eruption. This provides a minimum bound on the bubble trap vapor pressure since it must be greater than the exit pressure to drive flow out of the system. If we assume, for example, that the eruption conduit has a head of ~10 m, then hydrostatic pressure in the bubble trap will be ~0.2 MPa. Thus, pressures in the bubble trap are more than an order of magnitude greater than hydrostatic when flow is choked at the nozzle. Whereas saturation temperature for a hydrostatic pressure of ~0.2 MPa is ~120°C, at a pressure of ~1.2 MPa it rises to ~188°C, demonstrating that the saturated vapor pressure and temperature of bubble trap fluids increases dramatically in response to flow choking during an eruption. These high pressures and temperatures will significantly reduce the compressibility of the two-phase mixture in the reservoir (Figure S3.7), consistent with the decrease in flow oscillation period observed during eruption.

4.5. Similarity With Geophysical Signals Recorded in Active Volcanoes

Nearly three decades ago, it was proposed that *Volcanic seismicity that can specifically be attributed to activity of magma within conduits* (*in contrast to tectonic events or rock falls*, *for example*) *may have analogies in geyser systems that are amenable to detailed studies not possible at most volcanoes* [*Kieffer*, 1984]. Indeed, a multitude of signals recorded at Lone Star geyser resemble those measured in volcanic systems, in particular those generating Hawaiian and Strombolian eruptions. The similarities may provide insights into the role of aqueous fluids and gas slugs in the eruption process at volcanoes, and provide constraints for distinguishing between processes controlled by magma and those controlled by low viscosity and low-density aqueous fluids. Here we highlight some of our insights that could be used to interpret signals recorded at volcanoes and test or even improve physical models of volcanic processes.

The observed saw-tooth like tilt signals associated with Lone Star's eruptions (section 3.2) have similar forms to tilt transients recorded at Kilauea [*Anderson et al*., 2014] and Montserrat [*Costa et al*., 2013]. Both in Lone Star geyser and in these volcanoes the tilt transients record the mechanical response to periodic release of aqueous fluid or magma from a pressurized source. While in the Kilauea case, the resistance to magma liberation mainly originates from the mechanical behavior of the surrounding rocks, in Lone Star geyser the hydraulic head blocks the system until an extensive water phase change increases the volume and pressure that leads to the emptying of the cavity.

Several mechanisms have been proposed for producing VLP and ULP seismic signals that are now widely recorded at active volcanoes. A common feature of models for volcanic VLP signals is that they invoke an identical, repetitive source process, indicating a nondestructive source mechanism, produced by mass (and heat) advection in deformable conduits [e.g., *Chouet et al*., 2003; *Kazahaya et al*., 2011; *Lyons and Waite*, 2011; *Patrick et al*., 2011; *Sanderson et al*., 2010]. For example, VLP data recorded during the 1997 explosive activity at Stromboli Volcano in Italy was modeled as volumetric changes in conduits produced by

the piston-like action of the magma as a gas slug transited through variable conduit geometries [*Chouet et al*., 2003]. The repetitive nature of the ULP signals at Lone Star we attribute to gas slugs may thus have a magmatic equivalent. Episodic and self-similar ultralong period (ULP) signals coincident with eruptive activity and gas venting were recorded near the active vent at Santiaguito Volcano in Guatemala [*Sanderson et al*., 2010]. Similar to the signal in Lone Star, the ULP signals were associated with long-period rotational motion rather than horizontal translation. The source of the ULP signals, modeled as a Mogi point source, was offset from the center of the vent, similar to the offset cavity in Lone Star. The similarity between the signals and inferred processes in Santiaguito Volcano and Lone Star geyser implies that in both systems depressurization of the underlying system is dominated by episodic transport of heat and mass from a reservoir laterally offset from the vent, which may function as a bubble trap [*Belousov et al*., 2013], through fractures with complex geometries, to the surface.

The deformation associated with the Lone Star geyser eruption cycle recorded on all tiltmeters surrounding the geyser cone (Figure 1) is a reminder that geothermal systems can also be the source of deformation at volcanoes. Several numerical modeling studies have demonstrated that multiphase flow transients in the shallow hydrothermal system might be the source of observed vertical displacements in some calderas rather than magma intrusion [*Hurwitz et al*., 2007; *Hutnak et al*., 2009; *Todesco*, 2009; *Rinaldi et al*., 2010; *Fournier and Chardot*, 2012].

4.6. Future Studies

In order to better characterize the subsurface fracture and conduit geometry as well as multiphase fluid dynamics of geysers, it will be helpful to deploy dense seismometer and perform electrical resistivity tomographies. High spatial-resolution gravity measurements may be helpful as well, although results from our study suggest that gravity signals may be small. Ground Penetrating Radar might provide information on the very shallow (a few meters) structures in the subsurface, and LiDAR and ground-based radar interferometry surveys at high temporal resolution could provide images of ground deformation patterns at high spatial resolution, which in turn could improve constraints on the location of pressure sources. Contemporaneous measurements of pressure and temperature evolution in geyser conduits are needed to guide the development of coupled thermodynamic and fluid dynamic models. In order to comprehend the multiphase fluid dynamics of geyser systems, it will be necessary to improve our understanding of heat transfer between the different components of the geyser system, the conversion of heat to mechanical energy, and the properties of two-phase fluids [*Lu and Kieffer*, 2009]. In particular, we need to understand how these fluids behave during flow across nozzles, how and when they cavitate, and what is their compressibility.

5. Conclusions

On the basis of this study we conclude the following:

1. Periodic signals observed over 32 consecutive eruption cycles by multiple instruments include a 3:00 ± 0:16 h eruption interval, ULPs with durations of ~4 min and intervals of ~26 ± 8 min, internal flow oscillations with periods of ~60 s during preplay and ~30 s during relaxation, and 1–30 Hz hydrothermal tremor.
2. Lone Star geyser generates continuous hydrothermal tremor, representing collapse and/or nucleation of vapor bubbles, from a region to the northeast of the eruption conduit that is presumed to coincide with the location of a subsurface reservoir (bubble trap). The tremor is concentrated in two main frequency bands, 1–8 Hz and 15–25 Hz that did not vary during the 4 day experiment.
3. Pulses of high-amplitude tremor are generated from a location beneath the geyser conduit during times when fluids are being discharged from the vent (preplay and eruption). These high-amplitude pulses likely represent cavitation induced by the pressure drop associated with water discharge from the system. The systematically decreasing time delay between fluid discharge and tremor onset leading up to the eruption during the preplay stage is interpreted to result from steadily increasing geyser conduit temperatures during this phase of the eruption cycle.
4. The ULP signals appear to be independent from the geyser eruption cycle (i.e., ULPs occur randomly during all stages of the eruption cycle). We interpret these seismic signals as the passage of liquid and vapor slugs through the shallow crust in the study area, which modifies local pore pressures but otherwise does not affect the geyser system.

5. We model the flow oscillations of 30–60 s as resulting from the dynamical behavior of a mass-spring system, where the hydrostatic load in the geyser conduit represents the mass, and a compressible, two-phase (vapor/liquid) mixture in the bubble trap acts as the spring. These oscillations play a role in the preeruptive dynamics as they produce large dynamic changes of hydrostatic pressure in the system that favor cavitation boiling.
6. We attribute the geyser's dynamical behavior to thermomechanical coupling between the geyser conduit and a laterally offset reservoir (bubble trap) that stores energy in the form of compressed fluid. Eruptions occur when a nonlinear feedback between unloading of the system (via water discharge) and vapor generation (via cavitation) is initiated that accelerates vertical fluid velocities in the geyser conduit. This unstable situation is arrested by flow choking at a constriction/nozzle in the eruption conduit [*Karlstrom et al*., 2013], which in turn generates high pressures (>1.2 MPa) and temperatures (>188°C) upstream of the nozzle.
7. The subsurface dynamical processes associated with the geyser eruption cycle generate systematic, but heterogeneous, patterns of ground surface deformation. The average deformation pattern is consistent with gradual pressurization and inflation of the system leading up to an eruption, and rapid depressurization and deflation associated with mass discharge during an eruption.

Appendix A: Dynamics of Bubble Collapse due to Condensation in a Subcooled Liquid

As described in *Florschuetz and Chao* [1965], the relative importance of inertial versus thermal effects on a vapor bubble collapsing due to condensation is described by the dimensionless parameter:

$$B = Ja^2 \frac{\kappa_{TL}}{R_0} \sqrt{\frac{\rho_L}{p_\infty - p_{\mathrm{sat}}(T_\infty)}}, \tag{A1}$$

where κ_{TL} is the thermal diffusivity of the liquid, R_0 is the bubble radius, ρ_L is the liquid density, p_∞ is the ambient fluid pressure, $p_{\mathrm{sat}}(T_\infty)$ is the vapor saturation pressure at the ambient fluid temperature, and *Ja* is the dimensionless Jacob number representing the degree of subcooling of the liquid. *Ja* is given by

$$Ja = \frac{\rho_L}{\rho_V} \frac{c_{pL}(T_{\mathrm{sat}}(p_\infty) - T_\infty)}{h_{fg}}, \tag{A2}$$

where c_{pL} is the specific heat of the liquid, ρ_v is the vapor density, h_{fg} is the latent heat of evaporation, $T_{\mathrm{sat}}(p_\infty)$ is the vapor saturation temperature at the ambient fluid pressure, and T_∞ is the ambient fluid temperature.

Assuming that the vapor enters the system through a bubble trap as part of an equilibrium, two-phase (liquid/vapor) mixture, then the bubble trap liquids should be at temperatures close to saturation values. Thus, large degrees of subcooling are not expected. If we assume that the bubble trap is located at a depth of ~10 m and that the ambient pressure is equal to the equivalent hydrostatic load, then we have $p_\infty \sim 0.2$ MPa and $T_{\mathrm{sat}}(p_\infty) \sim 120$°C. For a small degree (~30°C) of subcooling, we have $T_\infty = 90$°C and $p_{\mathrm{sat}}(T_\infty) = 0.07$ MPa. Under these pressure and temperature conditions, $\rho_L = 943$ kg/m^3, $c_{p,L} = 4.2$ kJ/kg K, $\kappa_{T,L} = 1.67 \times 10$–7 m^2/s, $\rho_V = 1.129$ kg/m^3, and $h_{fg} = 2706$ kJ/kg. The only parameter we cannot constrain with thermodynamic properties is the bubble radius, R_0; and when these values are substituted into equations (A1) and (A2), we find that $B = 2.15 \times 10^{-5}/R_0$. Inertial mode (tremor-generating) collapse occurs for $B > 0.3$ or in this case for $R_0 < 0.076$ mm. Conversely, thermal mode (gentle) collapse occurs for $B < 0.003$ or in this case for $R_0 > 7.6$ mm. The Jakob number for this subcooling scenario is ~39, which, in general, is not high enough for inertial mode oscillations [*Chen and Mayinger*, 1992]. The *B* parameter calculations agree with this conclusion in that vapor bubbles entering the system are expected to have radii significantly larger than 0.12 mm. As a check, we repeated the above calculations assuming a very large degree of subcooling (~110°C), with $T_\infty = 10$°C (*Ja* ~143), which is perhaps the most extreme scenario imaginable. This scenario leads to $B > 0.3$ for $R_0 < 0.77$ mm and $B < 0.003$ for $R_0 > 77$ mm. These limiting bubble sizes are within the range expected at Lone Star, indicating that transitional dynamic behavior likely occurs for extreme degrees of subcooling. It is thus possible that low-amplitude tremor could be generated under this extreme (and unlikely) subcooling scenario. We conclude that vapor condensation in a subcooled liquid is unlikely to generate hydrothermal tremor under expected pressure-temperature conditions, but that tremor generation may be possible under extreme subcooling conditions.

Acknowledgments

We thank Doug Myren, Claire Pontbriand, Erin Looby, and Nellie Olsen for their assistance with the field work, and Stacey Gunther and Christie Hendrix for their assistance acquiring a research permit to work in Yellowstone National Park. Funding for USGS team members was provided by the USGS Volcano Hazards Program. R. Sohn's participation was supported by the WHOI Green Technology Program. M. Manga, L. Karlstrom and M. Rudolph did receive salary from the National Science Foundation to spend time on this project. We thank John Lyons, an anonymous reviewer, and Robert Lowell for helpful and constructive reviews. The data sets used in this paper are available upon request from the authors.

References

Adelstein, E., A. Tran, C. Munoz, A. Steinberg, and M. Manga (2014), Geyser preplay and eruption in a laboratory model with a bubble trap, *J. Volcanol. Geotherm. Res.*, *285*, 129–135, doi:10.1016/j.jvolgeores.2014.08.005.

Anderson, K., M. Poland, J. Johnson, and A. Miklius (2014), Episodic deflation-inflation events at Kīlauea Volcano and implications for the shallow magma system, in *Hawaiian Volcanism: From Source to Surface*, *Geophys. Monogr. Ser.*, vol. 208, edited by R. Carey et al., AGU, Washington, D. C., in press.

Anderson, L. W., J. W. Anderegg, and J. E. Lawler (1978), Model geysers, *Am. J. Sci.*, *278*, 725–738.

Baiter, H.-J., F. Gruneis, and P. Tilmann (1982), An extended base for the statistical description of cavitation noise, in *Proc. ASME Int. Symp. on Cavitation Noise*, pp. 93–108, ASME, Phoenix, Ariz.

Balmforth, N. J., R. V. Craster, and A. C. Rust (2005), Instability in flow through elastic conduits and volcanic tremor, *J. Fluid Mech.*, *527*, 353–377, doi:10.1017/S0022112004002800.

Belousov, A., M. Belousova, and A. Nechayev (2013), Video observations inside conduits of erupting geysers in Kamchatka, Russia, and their geological framework: Implications for the geyser mechanism, *Geology*, *41*, 387–390, doi:10.1130/G33366.1.

Birch, F., and G. C. Kennedy (1972), *Notes on Geyser Temperatures in Iceland and Yellowstone National Park*, *Geophys. Monogr. Ser.*, vol. 16, pp. 329–336, AGU, Washington, D. C.

Blake, J. R., and D. C. Gibson (1981), Growth and collapse of a vapour cavity near a free surface, *J. Fluid Mech.*, *111*, 123–140.

Blake, J. R., B. B. Taib, and G. Doherty (1987), Transient cavities near boundaries part 2. Free surface, *J. Fluid Mech.*, *181*, 197–212.

Brennen, C. E. (1995), *Cavitation and Bubble Dynamics*, Oxford Univ. Press, New York.

Bunsen, R. (1847), Physikalische beobachtungen ueber die haupt-saechliche Geysir Islands, *Poggendorffs Ann. Phys.Chem.*, *83*, 159–170.

Chen, Y. M., and F. Mayinger (1992), Measurement of heat transfer at the phase interface of condensing bubbles, *Int. J. Multiphase Flow*, *18*(6), 877–890.

Chouet, B. (2013), Introduction to quantitative volcano seismology: Fluid-driven sources, in *Modeling Volcanic Processes: The Physics and Mathematics of Volcanism*, edited by S. A. Fagents, T. K. P. Gregg, and R. M. C. Lopes, pp. 331–358, Cambridge Univ. Press, Cambridge, U. K.

Chouet, B., P. Dawson, T. Ohminato, M. Martini, G. Saccorotti, F. Giudicepietro, G. De Luca, G. Milana, and R. Scarpa (2003), Source mechanisms of explosions at Stromboli Volcano, Italy, determined from moment-tensor inversions of very-long-period data, *J. Geophys. Res.*, *108*(B1), 2019, doi:10.1029/2002JB001919.

Chouet, B., P. Dawson, and A. Arciniega-Ceballos (2005), Source mechanism of Vulcanian degassing at Popocatépetl Volcano, Mexico, determined from waveform inversions of very long period signals, *J. Geophys. Res.*, *110*, B07301, doi:10.1029/2004JB003524.

Costa, A., G. Wadge, R. Stewart, and H. Odbert (2013), Coupled subdaily and multiweek cycles during the lava dome eruption of Soufriere Hills Volcano, Montserrat, *J. Geophys. Res. Solid Earth*, *118*, 1895–1903, doi:10.1002/jgrb.50095.

Cros, E., P. Roux, J. Vandemeulebrouck, and S. Kedar (2011), Locating hydrothermal acoustic sources at Old Faithful Geyser using Matched Field Processing, *Geophys. J. Int.*, *187*, 385–393, doi:10.1111/j.1365-246X.2011.05147.x.

Dowden, J., P. Kapadia, G. Brown, and H. Rymer (1991), Dynamics of a geyser eruption, *J. Geophys. Res.*, *96*, 18,059–18,071, doi:10.1029/91JB01584.

Falanga, M., and S. Petrosino (2012), Inferences on the source of long-period seismicity at Campi Flegrei from polarization analysis and reconstruction of the asymptotic dynamics, *Bull. Volcanol.*, *74*, 1537–1551.

Florschuetz, L. W., and B. T. Chao (1965), On the mechanics of vapor bubble collapse, *J. Heat Transfer*, *87*, 209–220.

Fournier, N., and L. Chardot (2012), Understanding volcano hydrothermal unrest from geodetic observations: Insights from numerical modeling and application to White Island volcano, New Zealand, *J. Geophys. Res.*, *117*, B11208, doi:10.1029/2012JB009469.

Fournier, R. O. (1969), Old Faithful: A physical model, *Science*, *163*, 304–305.

Fournier, R. O. (1989), Geochemistry and dynamics of the Yellowstone National Park hydrothermal system, *Annu. Rev. Earth Planet. Sci.*, *17*, 13–53, doi:10.1146/annurev.ea.17.050189.000305.

Genco, R., and M. Ripepe (2010), Inflation-deflation cycles revealed by tilt and seismic records at Stromboli volcano, *Geophys. Res. Lett.*, *37*, L12302, doi:10.1029/2010GL042925.

Grant, M. A., and M. L. Sorey (1979), The compressibility and hydraulic diffusivity of a water-steam flow, *Water Resour. Res.*, *15*, 684–686, doi:10.1029/WR015i003p00684.

Hurwitz, S., and J. B. Lowenstern (2014), Dynamics of the Yellowstone hydrothermal system, *Rev. Geophys.*, *52*, 375–411, doi:10.1002/2014RG000452.

Hurwitz, S., L. B. Christiansen, and P. Hsieh (2007), Hydrothermal fluid flow and deformation in large calderas: Inferences from numerical simulations, *J. Geophys. Res.*, *112*, B02206, doi:10.1029/2006JB004689.

Hurwitz, S., A. Kumar, R. Taylor, and H. Heasler (2008), Climate-induced variations of geyser periodicity in Yellowstone National Park, USA, *Geology*, *36*, 451–454, doi:10.1130/G24723A.1.

Hurwitz, S., A. G. Hunt, and W. C. Evans (2012), Temporal variations of geyser water chemistry in the Upper Geyser Basin, Yellowstone National Park, USA, *Geochem. Geophys. Geosyst.*, *13*, Q12005, doi:10.1029/2012GC004388.

Hurwitz, S., R. A. Sohn, K. Luttrell, and M. Manga (2014), Triggering and modulation of geyser eruptions in Yellowstone National Park by earthquakes, Earth tides, and weather, *J. Geophys. Res. Solid Earth*, *119*, 1718–1737, doi:10.1002/2013JB010803.

Hutchinson, R. A., J. A. Westphal, and S. W. Kieffer (1997), In situ observations of Old Faithful Geyser, *Geology*, *25*, 875–878.

Hutnak, M., S. Hurwitz, S. E. Ingebritsen, and P. Hsieh (2009), Numerical models of caldera deformation: Effects of multi-phase and multi-component hydrothermal fluid flow, *J. Geophys. Res.*, *114*, B04411, doi:10.1029/2008JB006151.

Ichihara, M., and T. Nishimura (2009), Pressure impulses generated by bubbles interacting with ambient perturbation, in *Extreme Environmental Events: Complexity in Forecasting and Early Warning*, edited by R. A. Meyers, pp. 731–752, Springer, New York.

Ingebritsen, S. E., and S. A. Rojstaczer (1993), Controls on geyser periodicity, *Science*, *262*, 889–892, doi:10.1126/science.262.5135.889.

Ingebritsen, S. E., and S. A. Rojstaczer (1996), Geyser periodicity and the response of geysers to deformation, *J. Geophys. Res.*, *101*, 21,891–21,905, doi:10.1029/96JB02285.

James, M. R., S. J. Lane, B. A. Chouet, and J. S. Gilbert (2004), Pressure changes associated with the ascent and bursting of gas slugs in liquid-filled vertical and inclined conduits, *J. Volcanol. Geotherm. Res.*, *129*, 61–82, doi:10.1016/S0377-0273(03)00232-4.

James, M. R., S. J. Lane, and B. A. Chouet (2006), Gas slug ascent through changes in conduit diameter: Laboratory insights into a volcano-seismic source process in low-viscosity magmas, *J. Geophys. Res.*, *111*, B05201, doi:10.1029/2005JB003718.

Kanamori, H., and J. W. Given (1982), Analysis of long-period waves excited by the May 18, 1980, eruption of Mount St. Helens—A terrestrial monopole?, *J. Geophys. Res.*, *87*, 5422–5432, doi:10.1029/JB087iB07p05422.

Karlstrom, L., S. Hurwitz, R. A. Sohn, J. Vandemeulebrouck, F. Murphy, M. L. Rudolph, M. J. S. Johnston, M. Manga, and R. B. McCleskey (2013), Eruptions at Lone Star Geyser, Yellowstone National Park, USA, part 1: Energetics and eruption dynamics, *J. Geophys. Res. Solid Earth*, *118*, 4048–4062, doi:10.1002/jgrb.50251.

Kazahaya, R., T. Mori, M. Takeo, T. Ohminato, T. Urabe, and Y. Maeda (2011), Relation between single very-long-period pulses and volcanic gas emissions at Mt. Asama, Japan, *Geophys. Res. Lett.*, *38*, L11307, doi:10.1029/2011GL047555.
Kedar, S., B. Sturtevant, and H. Kanamori (1996), The origin of harmonic tremor at Old Faithful geyser, *Nature*, *379*, 708–711, doi:10.1038/379708a0.
Kedar, S., H. Kanamori, and B. Sturtevant (1998), Bubble collapse as the source of harmonic tremor at Old Faithful Geyser, *J. Geophys. Res.*, *103*, 24,283–24,299, doi:10.1029/98JB01824.
Kieffer, S. W. (1984), Seismicity at Old Faithful Geyser: An isolated source of geothermal noise and possible analogue of volcanic seismicity, *J. Volcanol. Geotherm. Res.*, *22*, 59–95, doi:10.1016/0377-0273(84)90035-0.
Kieffer, S. W. (1989), Geologic nozzles, *Rev. Geophys.*, *27*, 3–38, doi:10.1029/RG027i001p00003.
Le Conte, J. (1878), Geysers and how they are explained, *Pop. Sci. Mon.*, *12*(4), 407–417.
Lu, X., and S. W. Kieffer (2009), Thermodynamics and mass transport in multicomponent, multiphase H_2O systems of planetary interest, *Annu. Rev. Earth Planet. Sci.*, *37*, 449–477.
Lyons, J. J., and G. P. Waite (2011), Dynamics of explosive volcanism at Fuego volcano imaged with very long period seismicity, *J. Geophys. Res.*, *116*, B09303, doi:10.1029/2011JB008521.
Lyons, J. J., G. P. Waite, M. Ichihara, and J. M. Lees (2012), Tilt prior to explosions and the effect of topography on ultra-long-period seismic records at Fuego volcano, Guatemala, *Geophys. Res. Lett.*, *39*, L08305, doi:10.1029/2012GL051184.
Mackenzie, G. S. (1811), *Travels in the Island of Iceland*, 27 pp., Allam and Company, Edinburgh.
Maeda, Y., and M. Takeo (2011), Very-long-period pulses at Asama volcano, central Japan, inferred from dense seismic observations, *Geophys. J. Int.*, *185*, 265–282, doi:10.1111/j.1365-246X.2011.04938.x.
Maeda, Y., H. Kumagai, R. Lacson Jr., M. S. Figueroa II, and T. Yamashina (2013), Source process of long-period seismic events at Taal volcano, Philippines: Vapor transportation and condensation in a shallow hydrothermal fissure, *J. Geophys. Res. Solid Earth*, *118*, 2832–2846, doi:10.1002/jgrb.50205.
Mogi, K. (1958), Relations between the eruptions of various volcanoes and the deformation of the ground surfaces around them, *Bull. Earthquake Res. Inst. Tokyo*, *36*, 99–134.
Montalbetti, J. R., and E. R. Kanasevich (1970), Enhancement of teleseismic body phase with a polarization filter, *Geophys. J. R. Astron. Soc.*, *21*, 119–129.
Morozov, V. P. (1969), Cavitation noise as a train of sound pulses generated at random times, *Sov. Phys. Acoust.*, *14*, 361–365.
Namiki, A., C. Munoz-Saez, and M. Manga (2014), El Cobreloa: A geyser with two distinct eruption styles, *J. Geophys. Res. Solid Earth*, *119*, 6229–6248, doi:10.1002/2014JB011009.
Nicholls, H. R., and J. S. Rinehart (1967), Geophysical study of geyser action in Yellowstone National Park, *J. Geophys. Res.*, *72*, 4651–4663, doi:10.1029/JZ072i018p04651.
Nishimura, T., M. Ichihara, and S. Ueki (2006), Investigation of the Onikobe geyser, NE Japan, by observing the ground tilt and flow parameters, *Earth Planets Space*, *58*, 21–24.
Ohminato, T. (2006), Characteristics and source modeling of broadband seismic signals associated with the hydrothermal system at Satsuma-Iwojima volcano, Japan, *J. Volcanol. Geotherm. Res.*, *158*, 467–490, doi:10.1016/j.jvolgeores.2006.08.004.
Ohminato, T., B. A. Chouet, P. Dawson, and S. Kedar (1998), Waveform inversion of very long period impulsive signals associated with magmatic injection beneath Kilauea volcano, Hawaii, *J. Geophys. Res.*, *103*, 23,839–23,862, doi:10.1029/98JB01122.
Patrick, M., D. Wilson, D. Fee, T. Orr, and D. Swanson (2011), Shallow degassing events as a trigger for very-long-period seismicity at Kīlauea Volcano, Hawai'i, *Bull. Volcanol.*, *73*, 1179–1186, doi:10.1007/s00445-011-0475-y.
Rayleigh, L. (1917), On the pressure developed in a liquid during the collapse of a spherical cavity, *Philos. Mag. J. Sci.*, *34*, 94–98.
Rinaldi, A. P., M. Todesco, and M. Bonafede (2010), Hydrothermal instability and ground displacement at the Campi Flegrei caldera, *Phys. Earth Planet. Inter.*, *178*, 155–161, doi:10.1016/j.pepi.2009.09.005.
Rinehart, J. S. (1965), Earth tremors generated by Old Faithful Geyser, *Science*, *150*, 494–496, doi:10.1126/science.150.3695.494.
Rojstaczer, S., D. L. Galloway, S. E. Ingebritsen, and D. M. Rubin (2003), Variability in geyser eruptive timing and its causes: Yellowstone National Park, *Geophys. Res. Lett.*, *30*(18), 1953, doi:10.1029/2003GL017853.
Rudolph, M. L., M. Manga, S. Hurwitz, M. J. Johnston, L. Karlstrom, and C.-Y. Wang (2012), Mechanics of Old Faithful Geyser, Calistoga, California, *Geophys. Res. Lett.*, *39*, L24308, doi:10.1029/2012GL054012.
Rust, A. C., N. J. Balmforth, and S. Mandre (2008), The feasibility of generating low-frequency volcano seismicity by flow through a deformable channel, in *Fluid Motions in Volcanic Conduits: A Source of Seismic and Acoustic Signals*, edited by S. J. Lane and J. S. Gilbert, *Geol. Soc. London Spec. Publ., 307*, 45–56.
Sanderson, R. W., J. B. Johnson, and J. M. Lees (2010), Ultra-long period seismic signals and cyclic deflation coincident with eruptions at Santiaguito volcano, Guatemala, *J. Volcanol. Geotherm. Res.*, *198*, 35–44, doi:10.1016/j.jvolgeores.2010.08.007.
Shteinberg, A., M. Manga, and E. Korolev (2013), Measuring pressure in the source region for geysers, Geyser Valley, Kamchatka, *J. Volcanol. Geotherm. Res.*, *264*, 12–16.
Steinberg, G. S., A. G. Merzhanov, and A. S. Steinberg (1981), Geyser process: Its theory, modeling and field experiment, part 1. Theory of the geyser process, *Mod. Geol.*, *8*, 67–70.
Steinberg, G. S., A. G. Merzhanov, A. S. Steinberg, and A. A. Rasina (1982), Geyser process: Its theory, modeling and field experiment, part 2. A laboratory model of a geyser, *Mod. Geol.*, *8*, 71–74.
Thiéry, R., and L. Mercury (2009), Explosive properties of water in volcanic and hydrothermal systems, *J. Geophys. Res.*, *114*, B05205, doi:10.1029/2008JB005742.
Todesco, M. (2009), Signals from the Campi Flegrei hydrothermal system: Role of a "magmatic" source of fluids, *J. Geophys. Res.*, *114*, B05201, doi:10.1029/2008JB006134.
Toramaru, A., and K. Maeda (2013), Mass and style of eruptions in experimental geysers, *J. Volcanol. Geotherm. Res.*, *257*, 227–239, doi:10.1016/j.jvolgeores.2013.03.018.
Vandemeulebrouck, J., P. Roux, and E. Cros (2013), The plumbing of Old Faithful Geyser revealed by hydrothermal tremor, *Geophys. Res. Lett.*, *40*, 1989–1993, doi:10.1002/grl.50422.
Waite, G. P., P. A. Nadeau, and J. J. Lyons (2013), Variability in eruption style and associated very long period events at Fuego volcano, Guatemala, *J. Geophys. Res. Solid Earth*, *118*, 1526–1533, doi:10.1002/jgrb.50075.
White, D. E. (1967), Some principles of geyser activity, mainly from Steamboat Springs, Nevada, *Am. J. Sci.*, *265*, 641–684.
White, D. E., R. O. Fournier, L. J. P. Muffler, and A. H. Truesdell (1975), Physical results from research drilling in thermal areas of Yellowstone National Park, Wyoming, *U.S. Geol. Surv. Prof. Pap.*, *892*, 11–25.
Yoon, S. W., L. A. Crum, A. Prosperetti, and N. Q. Lu (1991), An investigation of the collective oscillations of a bubble cloud, *J. Acoust. Soc. Am.*, *89*, 700.